Cancer Theranostic Applications of Albumin-Coated Tobacco Mosaic Virus Nanoparticles

A. S. Pitek[†], **H. Hu**[†,‡], **S. Shukla**[†,‡], and **N. F. Steinmetz**[*,†,‡]

[†]Department of Biomedical Engineering, Case Western Reserve University, Cleveland, Ohio 44106, United States

[‡]Department of NanoEngineering, Moores Cancer Center, University of California, San Diego, San Diego, California 92093, United States

Abstract

Nanotechnology holds great promise in cancer drug delivery, and of particular interest are theranostic approaches in which drug delivery and imaging are integrated. In this work, we studied and developed the plant virus tobacco mosaic virus (TMV) as a platform nanotechnology for drug delivery and imaging. Specifically, a serum albumin (SA)-coated TMV formulation was produced. The SA coating fulfils two functions: SA provides a stealth coating for enhanced biocompatibility; it also acts as a targeting ligand enabling efficient tumor accumulation of SA-TMV versus TMV in mouse models of breast and prostate cancer. We demonstrate drug delivery of the chemotherapy doxorubicin (DOX); TMV-delivered DOX outperformed free DOX, resulting in significant delayed tumor growth and increased survival. Furthermore, we demonstrated the ability of SA-coated TMV loaded with chelated Gd(DOTA) for magnetic resonance imaging detection of tumors. In the future, we envision the application of such probes as theranostic, where first imaging is performed to assess whether the nanoparticles are effective at targeting a particular patient tumor. If targeting is confirmed, the therapeutic would be added and treatment can begin. The combination of imaging and therapy would allow to monitor disease progression and therefore inform about the effectiveness of the drug delivery approach.
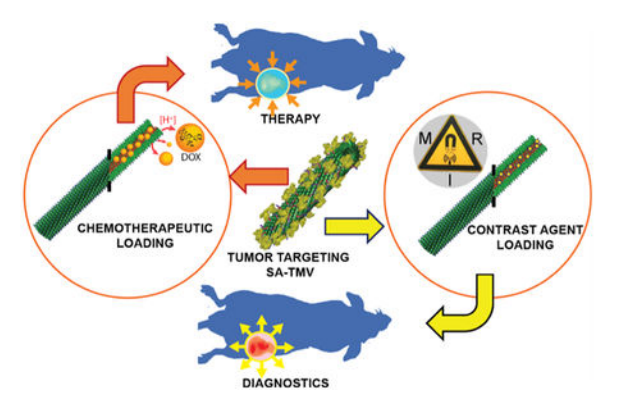
Graphical Abstract

Keywords

tobacco mosaic virus; cancer nanotechnology; drug delivery; imaging; theranostics

INTRODUCTION

Nanoparticle technologies find manifold applications targeting human health. A large library of nanoparticles is currently being developed and tested, and few examples have advanced into clinical trials and practice.[1] Nanoparticles come in many different shapes and sizes, and can be loaded with drugs or contrast agents as well as targeting ligands.[2] One of the many advantages that nanoparticle engineering provides is the possibility of tuning the carrier to a specific biological problem. In our research, we focus on nanoparticle biologics, specifically plant virus-based nanotechnologies. Although their mammalian counterparts have long been exploited as vaccines and gene delivery vectors,[3] plant virus-based nanotechnologies may offer some advantages; these include their ease of production in various homologous and heterologous expression systems using plants, bacteria, or insect cells.[4] Plant viruses are proteinaceous nanoparticles; their capsids are monodisperse, and many plant virus structures are known to near atomic resolution, therefore enabling structure-based design of high-precision delivery systems.[5]

In this work, we investigated theranostic applications of tobacco mosaic virus (TMV); specifically we evaluated its performance as a drug delivery vehicle and contrast agent. TMV is a soft matter, hollow nanotube measuring 300×18 nm with a 4 nm wide internal channel. Our previous research indicates that this high aspect ratio (AR = 18) is advantageous in the context of cancer nanotechnology, because elongated materials have favorable biodistribution and tumor homing capability as compared to spherical particles.[6] These results are matched with findings reported with synthetic nanotechnologies.[2] Another feature conferred by the high aspect ratio is the reduced nonspecific deposition in phagocytes,[7] which may help avoid or reduce potential immune responses against the carrier. In addition to its beneficial shape-related attributes, the chemistry and engineering of TMV is well characterized.[8,9] TMV offers chemically distinct interior and exterior surfaces, therefore allowing structure-based engineering of designer nanoparticles with various cargos loaded into the central channel, or conjugated and displayed on its exterior surface.[9] Making use of these attributes of TMV, we tested here its potential for targeted drug delivery and

imaging of solid tumors. Therapeutic particle formulations with the chemotherapy doxorubicin (DOX) attached via different chemistries were developed; Gd(DOTA)-loaded particles were also produced for tumor-imaging studies. Because our recent research demonstrated enhanced biocompatibility of TMV coated with serum albumin (SA),[10] in the current study we considered SA-coated versus "naked" or PEGylated TMV. SA is the most abundant protein in blood plasma, and as such, it makes a good candidate for camouflaging nanoparticles. Our previous work showed that SA-TMV had reduced antibody recognition[10] as well as increased circulation times.[11] Immunological evaluation of these particles revealed evasion from neutralizing antibodies, making SA-TMV an interesting candidate for further development for nano-oncology applications. Here, we report drug delivery and magnetic resonance imaging (MRI) using the SA-coated TMV-based carrier in mouse models of breast and prostate cancer.

RESULTS AND DISCUSSION

A panel of TMV-based nanoparticles was synthesized:

1. Fluorescently labeled TMV-Cy5 for biodistribution studies.

2. DOX-conjugated TMV for drug delivery studies; in particular, two distinct drug-carrying TMV particles were synthesized and studied: TMV-DOX and TMV−/−DOX carrying the chemotherapeutic DOX via a stable amide bond versus a pH-labile hydrazine bond, respectively.

3. TMV-Gd(DOTA) for MRI.

The therapeutic DOX and imaging agents Cy5 or Gd-(DOTA) were loaded into the central channel of TMV by targeting its Glu side chains (Glu 97/106).[9] In brief, azide-functional Cy5 and Gd(DOTA) were conjugated to TMV via Cu-catalyzed azide–alkyne cycloaddition (click) reaction after its modification with alkyne handles.[12] Therapeutic TMV formulations were obtained by conjugation of DOX via its amine groups to Glu side chains on the TMV channel, yielding a stable TMV-DOX formulation. Alternatively, DOX was reacted with the TMV particle following conjugation of a hydrazide handle yielding a pH-labile TMV−/−DOX formulation. At the same time, the exterior surface of TMV was modified with SA to enhance its in vivo performance. SA was conjugated using protocols previously developed by us. In brief, a thiol-PEG linker was introduced to the amines of SA, whereas a PEG-maleimide handle was conjugated to TMV; SA-TMV was then produced through Michael reaction. The chemical reactions are outlined in Figure 1A + B and detailed in the Experimental Section.

TMV-based nanoparticles were characterized using a combination of gel electrophoresis (SDS-PAGE), UV–vis spectroscopy, TEM, and dynamic light scattering (DLS) (Figure 1, Table 1). The SDS-PAGE revealed successful conjugation of SA to the surface of TMV, as evident by high molecular weight ($M_w > 64$ kDa) bands corresponding to the sum M_w of the TMV coat protein TMVcp (~17 kDa), SA (~66 kDa), and M_w of PEG linker (~0.7 kDa). ImageJ software and lane analysis tool indicated that approximately 342 ± 81 SA molecules were conjugated per TMV particle. It should be noted that in all samples, non-conjugated SA was also detectable (a protein band matching the molecular weight of SA). This is likely

because of the presence of non-covalently adsorbed SA rather than free SA, that is, free in solution and not associated with TMV. The non-covalently adsorbed SA is likely stacked onto TMV either via nonspecific protein–protein interactions or via SA dimerization. Overall, the characteristics of the SA-TMV formulation are in agreement with our previous studies in which SA-TMV was synthesized and studied.[10] Multiple protein bands were apparent in the (SA-)TMV−/−DOX samples, which may indicate some degree of cross-linking, which may be introduced through the reaction with homo-bifunctional AAD. Neither TEM (Figure S1) nor 3 DLS studies (Table 1) indicated aggregation; therefore, we argue that intraparticle cross-linking rather than interparticle cross-linking occurred. AAD could interlink two neighboring TMVcps via EDC conjugation to carboxyl groups on both ends of AAD.

Loading of Cy5 and DOX was quantified based on UV–vis measurements. Approximately 109 ± 12 Cy5 molecules were conjugated per TMV particle. Lastly, the therapeutic payload was determined at 1476 DOX per TMV-DOX and 1664 ± 282 DOX per TMV−/−DOX. Using similar conjugation strategies, one study reported the loading of 469 DOX per TMV via hydrazone bonds,[13] and another reported up to 5400 DOX per TMV via amide bonds.[14] The varying ratios can be explained by differences in the specific conjugation protocols and choice of purification; for example, we had previously found that up to 5400 DOX were conjugated to TMV; however, our data also indicated some non-covalent bonding of DOX to TMV under the conditions used in that study.[14] The lower loading of 469 DOX in a previous study and the 1664 DOX per TMV−/−DOX reported here may be explained by differences in molar excess used: in our study, 5 DOX per CP was used (details are provided in the Experimental Section), whereas 3 DOX per CP was used in the previous study.[13] Furthermore, it should be noted that we cannot rule out some DOX being attached to the exterior Lys side chains via Schiff base. In the context of other plant virus-based nanoparticle technologies, drug loading capacity appears rather consistent among the various platforms [potato virus X (PVX),[15] CPMV,[16] RCNMV,[17] with efficiencies on a "per molecular weight" basis, ranging within 1 and 5 wt %; this is generally comparable to drug formulations using liposomal or polymeric nanoparticles.

Last but not least, we used TEM and DLS to confirm the structural integrity of the particles: TEM images of SA-coated TMV-Cy5 and TMV−/−DOX reveal high aspect ratio TMV particles; it appears that SA-TMV−/−DOX has a higher tendency to align end to end on the TEM grids (Figure 1E); however, DLS did not indicate an increase in hydrodynamic radius, which may imply that the longer SA-TMV−/−DOX is an artifact caused by drying effects. DLS data indicate that TMV formulations remained intact (smaller hydrodynamic radii would be indicative of broken particles) with no apparent aggregation (which would be indicated by increased hydrodynamic radii). A slight decrease in hydrodynamic diameter for SA-TMV-Cy5/DOX was noted; because TEM did not indicate the presence of broken particles, the slightly lower hydrodynamic radii may be explained by better dispersion of SA-coated TMV particles in comparison to non-modified TMV-Lys, which tends to aggregate after long-term storage.

Overall, SA-coated therapeutic and fluorescent TMV particles were obtained; Gd(DOTA)-loaded TMV nanoparticles were also synthesized and are described below (see the MRI section).

Before testing the efficacy of the therapeutic TMV formulations, we set out to assess the biodistribution of TMV versus SA-TMV using mouse models of breast cancer: two heterotopic models were used—first the human MDA-MB-231 model in female NCR nu/nu mice, and second, the murine 4T1 model in female Balb/c mice. Fluorescent TMV particles were used; the particles were administered intravenously at a dose of 37.5 mg/kg (this dose was chosen because it equates to 1 mg/kg of DOX for the DOX-loaded TMV formulations, the dosing used for the subsequent drug delivery studies). Ten hours post-administration, mice were euthanized, and dissected and organs collected and imaged using the Maestro imager (Figure 2). The biodistribution pattern followed the general trend as we previously observed with TMV[18] and is also consistent with that of synthetic nanoparticles.[19] Clearance of the TMV particles occurs mostly through the liver and spleen, with 71–91% of the total fluorescence signals being observed from these organs. This is expected as liver and spleen are the major organs of the reticuloendothelial system responsible for clearance of macromolecular agents. TMV, but not SA-TMV, particles were observed to accumulate in lungs. We have previously observed this and also documented that multivalent IgM binds to TMV, leading to clustering and therefore accumulation in the lungs.[20] It should be noted that we mostly observe lung accumulation for the Lys-added mutant of TMV and not as much for the native TMV formulation; the TMV-Lys (used throughout this study) tends to aggregate more rapidly compared to native TMV (unpublished observations). The phenomenon that TMV-Lys is sequestered in the lungs is observed only in Balb/c mice and not in immunocompromised athymic mice, further indicating that indeed immune surveillance plays a role. SA-TMV particles were not found in the lungs attesting to the enhanced biocompatibility of the SA-TMV formulation. In fact, in our recent study we demonstrated that although stealth coating of TMV does not prevent the formation of anti-TMV IgG in mice after repeat administration, the SA coating effectively shields SA-TMV from immune recognition by these carrier-specific antibodies.[10]

Tumor accumulation of "naked" TMV was low in both mouse models studied ranging between 0 and 1% of the particles deposited in organs. In stark contrast, the SA-TMV formulations showed significant tumor accumulation with >2 and 9% in the MDA-MB-231 and 4T1 models, respectively (Figure 2). The enhanced tumor accumulation of SA-TMV versus "naked" TMV could be explained by the distinct biodistribution, with SA-TMV avoiding aggregation, which can lead to nonspecific sequestration of particles in the lung. Also, we have previously shown that SA coating on TMV increases its circulation half-life; although "naked" TMV had a plasma half-life of <10 min, SA-TMV was found to exhibit a 10-fold longer circulation half-life of ~100 min.[11] The increased circulation time may increase passive tumor homing. However, it is also possible that the enhanced tumor homing of SA-TMV versus TMV could be explained by an active targeting mechanism mediated by the SA coating. For example, the SA formulation of paclitaxel, Abraxane, has been thought to accumulate in tumors based on targeting the albumin transport receptor gp60.[21] Abraxane binding to gp60 translocates the nanoparticle drug into the tumor interstitium, where it may interact with SPARC, an albumin-binding protein that has been reported to be overexpressed

in tumors.[22–24] This is consistent with clinical studies that have shown that SPARC expression correlates to tumor response in head and neck cancer patients treated with Abraxane.[25] Therefore, active targeting and enhanced biocompatibility could explain the enhanced tumor homing capabilities of SA-TMV versus "naked" TMV.

We noted a significant difference in SA-TMV tumor homing comparing the two mouse models, with particle accumulation being higher in the mouse model bearing mouse (4T1) versus human (MDA-MB-231) tumors (Figure 2). In our experiments, all TMV formulations were coated with mouse-derived SA (MSA); to test whether the coating with human SA (HSA) would increase tumor homing of SA-TMV in the human MDA-MB-231 mouse model, we repeated the tumor homing study comparing MSA- and HSA-coated TMV. The results show near-perfect reproducibility of the data shown in Figure 2, and there were no statistically significant differences comparing tumor accumulation of MSA-TMV versus HSA-TMV (Figure S2). We also tested whether differences on a cellular level could be distinguished; cell uptake studies were performed but no differences were observed; both MSA- and HSA-TMV were taken up by MDA-MB-231 cells with comparable efficiencies (Figure S2A). Therefore, we hypothesize that the differences in tumor homing of the SA-coated TMV in the different mouse models are because of the differences in the tumor physiology rather than the species-specific protein coating.

Next, we investigated cancer cell uptake and cytotoxicity of "naked" versus SA-coated TMV carrying DOX conjugated via amide versus hydrazone bonds; again, the MDA-MB-231 and 4T1 cancer cell lines were studied. Interestingly, in cell culture conditions, SA coating of TMV significantly reduced its cell uptake properties, whereas uptake of free DOX and TMV-bound DOX were similar (Figure 3A,B). Reduced cell uptake of the SA-coated TMV particles also correlated with reduced cell killing efficacy (Figure 3C,D). Although TMV-DOX and TMV−/−DOX reached IC50 values ranging between 0.3 and 0.8 μM comparable to that of free DOX (0.3 μM for the 4T1 cell line and 2 μM for MDA-MB231 cells), SA-TMV-DOX and −/−DOX exhibited higher IC50 values with 1.5 and 6.2 μM for the MDA-MB-231 cells and 33.8 and 37 μM for the 4T1 cells. Although the in vitro results indicated reduced cell uptake for the SA-coated TMV formulations; in vivo biodistribution data indicated enhanced tumor targeting of the SA-coated TMV particles. Therefore, one may argue that SA-TMV accumulate in the tumor vasculature and tumor interstitium rather than in cancer cells themselves. This, in fact, may be a desired outcome because research has shown that tumor cell targeting can limit the penetration depth of the nanoparticle formulation into the tumor.[19] Therefore, targeting the tumor microenvironment (TME) more broadly could be beneficial for drug delivery.

Because data indicated low cell uptake of SA-TMV particles, we chosen the pH labile formulation for in vivo efficacy studies; while heterogeneic, the TME generally has an acidic pH, and others have shown that pH labile drugs are released within the TME.[26] Before moving into the in vivo studies, we confirmed that DOX indeed is released from SA-TMV−/−DOX particles under acidic conditions. SA-TMV−/−DOX formulations were incubated in 37 °C in buffered solutions at pH 5 and pH 6.5 for 6, 24, or 48 h and subsequently analyzed on agarose gels. Gels were imaged under UV light to detect DOX. TMV does not migrate in these agarose gels and, therefore, sits in the gel pockets; free DOX, however, migrates

toward the cathode and is detectable as fluorescent streaks in the gels (Figure 4). The results indicate that indeed at lower pH, DOX is released from the carrier; this effect is more profound at lower pH (pH 5 vs pH 6.5), and DOX release increased over time.

Next, we investigated the efficacy of SA-TMV–/–DOX in the MDA-MB-231 tumor-bearing athymic mouse model. Treatments were started when the tumor volume reached 100–160 mm^3. The dosage of DOX for either SA-TMV–/–DOX or free DOX was 1 mg per kg body weight. Intravenous injections into the tail vein were given every 3 days, and a total of 10 treatments were given over a time course of 4 weeks. Tumor volumes were measured daily. With this treatment schedule, free DOX had no effect on tumor burden or survival (Figure 5). In stark contrast, the treatment arm receiving SA-TMV–/– DOX showed significant delay in tumor growth, which also lead to increased survival, with 80% of the animals remaining alive at day 40 when the study was terminated (Figure 5B).

Although several drug-loaded plant virus-based systems have been reported in the literature, only a few studies have investigated their drug delivery potential in in vivo animal models. Similar to the study reported here, we have previously shown that DOX-loaded PVX outperforms free DOX in the MDA-MB-231 model.[15] We also showed that TMV carrying a platinum therapy (phenanthriplatin) was more efficacious compared to the free drug; this could be explained by the enhanced tumor accumulation of the drug when delivered by TMV.[18] A non-high aspect ratio platform that has been recently investigated for DOX delivery in vivo is the RCNMV particle; in this study the authors concluded that most enhanced pharmacologic and efficacy advantages were achieved by frequent administration of the DOX-loaded RCNMV at low DOX dosage (<1 mg/kg).[17] Although only a few in vivo studies with plant viral delivery systems have been conducted, the data indicate that this platform technology is worth pursuing. Critical future studies would be the side-by-side comparison with synthetic systems as well as translational research detailing the safety of the plant viral nanoplatform technology. Furthermore, we need to drive research toward more clinically relevant tumor models, such as patient-derived models and spontaneous models, and/or evaluate the efficacy of the approach in large animals. For example, we recently tested a plant virus immunotherapy approach in canine patients with spontaneous oral melanomas.[27]

Lastly, toward the development of theranostic approaches, we tested the ability of SA-TMV loaded with an MRI contrast agent for tumor imaging. Theranostic approaches are either those that utilize dual-functional agents that combine the functionalities of imaging and drug delivery, or those in which mono-functional agents are used sequentially. Regarding the latter, this could be a particularly powerful strategy to stratify whether a patient would qualify for a certain nanoparticle therapeutic or not. Tumors differ from patient to patient; although some patients may present with tumors suitable for nanoparticle-assisted drug delivery (i.e., enhanced permeability and reduced lymphatic drainage), others may not. Therefore, we envision that MRI (or other clinical modalities) could be used to assess whether the SA-TMV particles accumulate in the tumor of an individual patient, prior to choosing the same nanoparticle for drug delivery. Also, the contrast agent–loaded formulation would be useful for longitudinal imaging to assess progression of disease or treatment success. For proof of concept, we chose a mouse model of prostate cancer using

nu/nu mice with subcutaneous tumors derived from PC-3 cells. To enable imaging via a clinically relevant modality, TMV was labeled with Gd(DOTA) using our previously established click chemistry protocols.[28] Gd(DOTA) was conjugated to the central channel of TMV and SA was displayed on its exterior surface (Figure 1). The resulting SA-TMV-Gd(DOTA) were characterized using SDS-PAGE and TEM (Figure S3). Inductively coupled plasma–optical emission spectroscopy (ICP–OES) was used to determine the Gd content; ~633 Gd(DOTA) were conjugated per SA-TMV-Gd(DOTA). The relaxivity of SA-TMV-Gd(DOTA) was measured at 13.5 mM^{-1} s^{-1} (Figure S4), which is in good agreement with previous studies.[29,30] Compared to small molecule agents, for example, Gadovist or Magnevist, the SA-TMV-Gd(DOTA) formulation has a 3× higher relaxivity per Gd. The high relaxivity may be explained by the reduced tumbling rates of the macromolecular carrier agent; in combination with its multidendate nature, this yields contrast agents with excellent magnetic properties; that is, on a per-particle basis, SA-TMV-Gd(DOTA) has an r_1 of 8500 mM^{-1} s^{-1}.

For in vivo imaging, athymic nu/nu mice (n = 3) bearing PC-3 xenografts were used, and we tested the effectiveness of our TMV-based contrast agent for T_1-mapping MRI (Figure 6A). Consistent with the fluorescent imaging data in the breast cancer mouse models (see Figure 2), quantitative analysis of the T_1 relaxation times within the tumor ROI 6 h post TMV administration showed a significant increase in signal enhancement comparing the SA-TMV-Gd(DOTA) particles versus PEGylated controls with 25% versus 9% decrease of T_1 observed, respectively. Animals from either treatment arm showed recovery of the T_1 relaxation times at 24 h post-injection, indicating successful biodegradation and clearance of the proteinaceous contrast agents from the body. This is as desired; after the imaging session is complete, it is important for the agent to be cleared from the body. In a recent study using integrin-targeted TMV contrast agents loaded with a dysprosium (Dy), a T_2 MRI contrast agent, we also showed effective imaging of PC-3 prostate tumors in a mouse model,[31] indicating the suitability of TMV-based carriers for MR imaging.

To further validate the MRI data and assess the biodistribution of SA-TMV-Gd(DOTA) and to quantify tumor homing of the TMV-based contrast agents, organs and tumors were harvested and the Gd^{3+} content was determined by ICP–OES (Figure 6C). In agreement with the in vivo MRI data, tumor homing was more profound for the SA-TMV-Gd(DOTA) versus PEG-TMV-Gd(DOTA) formulation, with Gd content showing a fourfold increase in tumors isolated from animals treated with SA-TMV-Gd(DOTA) versus PEG-TMV-Gd(DOTA) [Gd content was determined at 11.32 ng/g tumor and 3.98 ng/g tumor for SA-TMV-Gd(DOTA) vs PEG-TMV-Gd(DOTA)]. Apart from the differences in tumor homing, the SA- and PEG-based TMV-Gd(DOTA) formulations followed the anticipated biodistribution profiles with clearance through liver and spleen. As discussed above, this overall trend is consistent with prior observations made using plant virus-based nano-particles or synthetic nanoparticles.

CONCLUSIONS

In conclusion, we developed a viral nanoparticle that contains the functionalities of targeting and shielding, both conferred through the SA coating, as well as medically relevant cargos,

namely, the chemotherapy DOX or the MRI contrast agent GdDOTA. We demonstrated the utility of the viral nano-medicine both for drug delivery and for imaging. The ability of SA-decorated TMV nanoparticles to home to breast and prostate cancer tumors in mouse models thereof was demonstrated. The enhanced tumor homing of SA-coated versus "naked" or PEGylated TMV may be explained by the enhanced biocompatibility of SA-coated TMV and the conferred molecular specificity to SA-specific proteins overexpressed in the tumor microenvironment. TMV-delivered chemotherapy (here DOX was used) outperformed free drug and significantly delayed tumor growth while increasing survival. At the same time, we showed the applicability of the TMV-based contrast agent for MR imaging of tumors.

The SA-coated and cargo-loaded TMV nanoparticle provides several opportunities for future clinical development; we envision that these therapeutic and magnetic TMV formulations could be used in combination to develop integrated theranostic approaches. For example, using the TMV contrast agent, one would first test whether the formulation indeed homes and accumulates at disease sites in a particular patient; then, one would put the patient on this therapeutic regimen. Multifunctional particle formulation may also be useful for longitudinal monitoring of disease progression and treatment efficacy using MRI imaging. The integration of imaging into novel drug trials is envisioned to be highly beneficial, as read-out could be provided in real time, therefore allowing to adjust the treatment regimen as needed (an opportunity not provided in end-point trials). It is still a long way toward the clinical realization of plant virus-based theranostics, but studies like this will pave the way toward this goal.

MATERIALS AND METHODS

Virus Propagation and Purification.

TMV-Lys[32] was propagated in *Nicotiana benthamiana* by mechanical inoculation using 5–10 μg of virus per leaf. The isolation of TMV-Lys using established procedures yielded approximately 1–7 mg of virus per gram of infected leaf material. TMV-Lys was used throughout all studies and will be referred to as TMV in the remainder of the text.

TMV Loading with Cy5, DOX or Gd(DOTA).

For Cy5 and Gd(DOTA) conjugation, first alkynes were attached to TMVs carboxylic acids on the solvent-exposed surface of the channel; 100 equiv of propargylamine (P50900; Sigma-Aldrich), 50 equiv of EDC (25 equiv added at 0 and 16 h; E6383; Sigma-Aldrich), and 15 equiv HOBt (Acros Organics) were added per coat protein (CP; each TMV particle consists of 2130 identical copies of a CP unit) in 100 mM 2-[4-(2-hydroxyethyl)piperazin-1-yl]ethanesulfonic acid (HEPES) buffer, pH 7.4 (at final TMV concentration of 1 mg/mL). The reaction was allowed to proceed for 20 h. TMV was purified by ultra-centrifugation at 160 500g (42 000 rpm using 50.2 Ti rotor, Beckman Coulter) for 3 h on a 40% (w/v) sucrose cushion in 10 mM potassium phosphate (KP) buffer pH 7.4. For Cy5 conjugation, an alkyne–azide click reaction was performed by adding 0.5 equiv of sulfo-cyanine5 azide dye (Cy5-azide, B3330; Lumiprobe) and 10 equiv of Gd(DOTA)-azide (B288; Macrocyclics) per CP using 2 mg/mL TMV in the presence of 1 mM $CuSO_4$ (AC423615000; Fisher), 2 mM aminoguanidine (AC36891025; Fisher), and 2 mM L-ascorbic acid (AC352681000; Fisher)

in 10 mM KP buffer pH 7.4 containing 10% (v/v) dimethyl sulfoxide (DMSO); the reaction was allowed to proceed for 30 min on ice. TMV was purified by ultracentrifugation as described above and resuspended in 10 mM KP buffer, pH 7.4, yielding a TMV concentration of 10 mg/mL. The final sample was subjected to a clearing spin using a tabletop centrifuge ($7500g$, 5 min) to remove aggregates.

Two DOX-carrying TMV formulations were produced: TMV-DOX (non-cleavable) and TMV−/−DOX (cleavable). For TMV-DOX, DOX was attached to TMVs carboxylic acids on the solvent-exposed surface of the channel to produce non-cleavable TMV-DOX; 40 equiv of DOX (Indofine), 40 equiv of EDC (20 equiv added at 0 and 16 h; Sigma-Aldrich), and 10 equiv HOBt (Acros Organics) were added per CP in 100 mM HEPES buffer, pH 7.0 (at final TMV concentration of 1 mg/mL). The reaction was allowed to proceed for 20 h. TMV was purified by ultracentrifugation at 160 500g (42 000 rpm using 50.2 Ti Rotor, Beckman Coulter) for 3 h on a 40% (w/v) sucrose cushion in 10 mM KP buffer (pH 7.4). For TMV−/−DOX, first, adipic acid dihydrazide (AAD) was attached to TMVs carboxylic acids on the solvent-exposed surface of the channel to yield hydra-TMV; 23 equiv of AAD (203310250; Acros Organics), 30 equiv of EDC (10 equiv added at 0 h after 30 min and after 14 h; E6383; Sigma-Aldrich), and 20 equiv HOBt (Acros Organics) were added per CP in 100 mM HEPES buffer, pH 7.4 (at final TMV concentration of 0.9–1 mg/mL). The reaction was allowed to proceed for 20 h. Hydra-TMV was purified by ultracentrifugation as described above. Subsequently, DOX was attached to hydra-TMV to yield TMV−/−DOX; 5 equiv of DOX was added per TMV CP in 10 mM KP buffer pH 7.0 containing 10% (v/v) DMSO (at final TMV concentration of 1 mg/mL). The reaction was allowed to proceed for 2 days in room temperature in the dark. TMV−/−DOX was briefly spun down at $500g$ to remove aggregates and purified by ultracentrifugation; then TMV−/−DOX was resuspended in 10 mM KP buffer, pH 7.0, at a concentration of 10 mg/mL; aggregates were removed by centrifugation at $7500g$ for 5 min.

Conjugation of SA to TMV.

Human or mouse SA (Sigma-Aldrich or Bioworld, respectively) was conjugated to the surface of TMV targeting Lys side chains. First, SA was conjugated with NHS-PEG$_4$-SAT (Thermo Fisher) at 1:1 ratio in phosphate buffered saline (PBS; 0.01 M Na$_2$HPO$_4$, 0.0018 M KH$_2$PO$_4$, 0.0027 M KCl and 0.137 M NaCl, pH 7.4) containing 10% (v/v) DMSO overnight at RT. To de-protect the thiol group, 0.5 M hydroxylamine, 25 mM EDTA in PBS, pH 7.2–7.5, was added at a final concentration of 10% (v/v) and incubated for 3 h at RT. Separately, TMV was conjugated with maleimide-PEG$_4$-NHS (Thermo Fisher) at 10 equiv of PEG per coat protein in 10 mM potassium phosphate buffer, pH 7.4, containing 10% (v/v) DMSO, for 3 h at RT. The resulting maleimide-PEG$_4$-TMV conjugates were purified twice through PD MiniTrap G-25 desalting columns (GE) and combined with previously prepared SA-PEG$_4$-SH at 6 equiv per CP and reacted overnight at RT to yield SA-TMV particles. The reaction was quenched by addition of excess glycine and L-cysteine for 1 h at RT. The resulting constructs were then purified by ultracentrifugation at 112 000g (50 000 rpm using TLA-55 rotor, Beckman Coulter) for 1 h on a 40% (w/v) sucrose cushion in PBS. The final samples were resuspended in PBS, pH 7.4, to yield a concentration of 10 mg/mL of SA-TMV; aggregates were removed by centrifugation at $7500g$ for 5 min.

Dynamic Light Scattering.

DLS measurements were performed using a 90plus instrument (Brookhaven Instruments Corporation) at a scattering angle $h = 90°$. Reported values are averaged values of five measurements over 1 min. Hydrodynamic diameters (D_h) and polydispersity indices (PDI) were calculated using the manufacturer's software.

UV–Vis Spectroscopy.

The concentrations of TMV and Cy5 dye and DOX loading were determined by the Beer–Lambert law using an extinction coefficient of TMV at 260 nm $\varepsilon_{TMV(260nm)} = 3$ mL mg^{-1} cm^{-1} (MW$_{TMV}$ = 39.4 MDa), extinction coefficient of Cy5 at 646 nm $\varepsilon_{Cy5(646nm)} = 271\,000$ M^{-1} cm^{-1} (MW$_{Cy5}$ = 747 Da), and extinction coefficient of DOX at 481 nm $\varepsilon_{DOX(481nm)} = 10\,410$ M^{-1} cm^{-1} (MW$_{DOX}$ = 580 Da).

Sodium Dodecyl Sulfate-Polyacrylamide Gel Electrophoresis.

TMV and SA-TMV carrier particles (20 μg) were denatured at 100 °C for 7 min in gel loading buffer [62.5 mM Tris-HCl pH 6.8, 2% (w/v) SDS, 10% (v/v) glycerol, 0.01% (w/v) bromophenol blue, 10% (v/v) 2-mercaptoethanol]. Denatured protein samples were then separated on 4–12% NuPAGE polyacrylamide gels in 1× MOPS running buffer (Invitrogen) at 200 V for 40 min. The gels were stained with Coomassie brilliant blue and visualized using an AlphaImager imaging system (Biosciences).

Agarose Gel Electrophoresis.

To confirm pH-triggered cleavage of DOX from SA-TMV–/–DOX particles, SA-TMV–/–DOX were incubated in 0.1 M KP or acetate buffer, pH 5.0, 6.5, or 7.5 (control) at 37 °C for 6 h, 1 day, or 2 days. Subsequently, the samples were loaded with 6× agarose loading dye (Fisher Scientific) onto a 0.8% (w/v) agarose gel in the amount corresponding to 1.5 μg of DOX (based on UV–vis); free DOX was used as control in the amount of 0.3–3 μg. The electrophoresis was performed at 100 V for 30 min in TBE. Gels were visualized under UV light and documented using an AlphaImager imaging system (Biosciences).

Transmission Electron Microscopy.

Particles at a concentration of 0.05 mg/mL (2 μL per grid) were adsorbed to carbon-coated copper grids (01754-F, Ted Pella), rinsed with deionized water, and negatively stained with 2% (w/v) uranyl acetate for 5 min before analysis with a Tecnai TF30 S/TEM at 300 kV.

Cell Uptake Experiments.

200 000 4T1 or MDA-MB231 cells (collected using enzyme-free Hank's-based Cell Dissociation Buffer; Fisher) were incubated with DOX, TMV-DOX, or SA-TMV-DOX normalized to 0.4 μg of DOX (or with 20 μg SA-TMV-Cy5) in complete cell culture medium [RPMI medium for 4T1 or Dulbecco's modified Eagle's medium (DMEM) for MDA-MB231; media supplemented with 10% fetal bovine serum and 1% (v/v) penicillin/streptomycin] in triplicates in 96-well plate for 6–20 h at 37 °C and 5% CO$_2$. Cells were washed twice with PBS and resuspended in 200 μL of PBS. The fluorescence of the samples

was then analyzed with use of Tecan Infinite M200 plate reader using λ_{ex} = 480 nm and λ_{em} = 575 nm.

MTT Cell Viability Assay.

2000 4T1 cells or 5000 MDA-MB231 cells were seeded per well in a 96-well plate in 100 μL complete DMEM or RPMI cell culture medium, respectively. After 24 h at 37 °C, 5% CO_2, an additional 100 μL medium containing DOX, TMV-DOX, SA-TMV-DOX, TMV−/−DOX, and SA-TMV−/−DOX was added at 3.2 nM to 2 μM DOX; studies were set up in triplicates. Equivalent quantities of TMV and SA-TMV particles were used as controls. The cells were exposed to the various nanoparticle formulations for 20 h at 37 °C, 5% CO_2, after which the nanoparticle solution was replaced with 100 μL fresh medium; then, cells were incubated at 37 °C, 5% CO_2, for additional 20 or 48 h for 4T1 and MDA-MB231 cells, respectively. Subsequently, the viability of the cells was quantified using colorimetric MTT assay (ATTC) following manufacturer protocol. A Tecan Infinite M200 plate reader was used for the read-out at λ = 570 nm. The absorbance of wells containing no cells was used as background and % viability was calculated as the ratio between absorbance of treated and non-treated cells × 100%.

In Vivo Biodistribution.

All animal studies were carried out using Institutional Animal Care and Use Committee–approved procedures. The biodistribution of SA-TMV-Cy5 particles was investigated in heterotopic models of breast cancer: human MDA-MB-231 cells in female NCR nu/nu mice and murine 4T1 cells in female Balb/c mice; n = 5. 7–8-week-old mice were kept on alfalfa-free diet for ~2 weeks prior to start of the study. NCR nu/nu or Balb/c mice were injected subcutaneously into the right flank using 2.5×10^6 MDA-MB231 or 2.5×10^5 4T1 cells, respectively, suspended in 100 μL of media and Matrigel (Corning) at a 1:1 ratio. After 2–3 weeks, SA-TMV-Cy5 or TMV-Cy5 were administered intravenously at a dose of 37.5 mg/kg body weight (approximately 1 mg TMV per mouse). Mice were euthanized after 10 h; organs were removed and imaged using the Maestro fluorescence imaging system (PerkinElmer, MA, USA).

In Vivo Efficacy.

All animal studies were carried out using Institutional Animal Care and Use Committee–approved procedures. Female NCR nu/nu mice were injected subcutaneously into the right flank using 2.5×10^6 MDA-MB231 cells suspended in 100 μL media and Matrigel (Corning) in a 1:1 ratio. Tumors were measured and total volume was calculated using the formula $v = \frac{l \times w^2}{2}$. The treatment was initiated when tumors reached 100–160 mm³. SA-TMV−/−DOX or DOX were administered intravenously at a dose of 1.0 mg DOX/kg body mass in 3-day intervals; PBS was used in control group; n = 4 (for PBS and DOX groups) or n = 5 (for SA-TMV−/−DOX group) animals were used. Tumors were measured and mice were weighed daily. Mice were euthanized 41 days post first treatment or when the tumor volume reached 1000 mm³.

Relaxivity and Quantitative T1 Mapping by MRI.

The ionic relaxivity of the TMV-Gd(DOTA) particles was tested at 37 °C using a Brukman Minispec mq60 relaxometer (60 MHz). The in vivo MRI studies were performed on the same Biospec 7 T scanner equipped with a 3 cm birdcage ^{1}H coil (Bruker, Erlangen, Germany). First, a multi-slice, T_2-weighted imaging sequence (RARE) was used to provide location information of the tubes with the following parameters: TE/TR = 24/3000 ms, RARE factor = 8, NAV = 1, 15 axial slices with 1.5 mm thickness, matrix size = 128 × 128, 30 × 30 mm field of view (FOV). Total acquisition time was 48 s. Next, single-slice, T_1 mapping was performed using a saturation-recovery-Look–Locker (SRLL) sequence, as previously described,[33] and a spiral read-out to accelerate acquisition. The spiral SRLL used single-slice, FA = 10°, TE = 3.5 ms, slice thickness 1.5 mm, NAV = 4 for in vivo scan and NAV = 1 for phantom scans, FOV = 30 × 30 mm, matrix size 128 × 128. 50 images that covered 5 s of the saturation recovery curve were acquired with an interval of 100 ms. Proton density (M0) images were acquired with TR = 2000 ms. Spiral trajectory of 32 interleaves with zero moment compensated was designed using the minimum-time gradient method and measured manually for reconstruction. The scan time for each average is 2 min and 40 s. During MR imaging, mice were anesthetized by isoflurane, respiration rate maintained at 70—80/min. Images were acquired before and after injection. T_1 mapping images were statistically analyzed using in-house-developed Matlab software (The MathWorks, Inc, Natick, MA, USA).

After completion of the imaging study, the mice were sacrificed; the tumor and major organs (brain, lung, heart, liver, spleen, and kidneys) were collected. The tissues were weighed and digested in concentrated nitric acid overnight and heated to 90 °C for a further 6 h before the Gd content was determined by 730-ES ICP–OES (Agilent Technologies, Santa Clara, CA, USA). Values are presented as means plus standard deviations for n = 3 mice per group.

Supplementary Material

Refer to Web version on PubMed Central for supplementary material.

ACKNOWLEDGMENTS

REFERENCES

(1). Lammers T; Kiessling F; Hennink WE; Storm G Drug targeting to tumors: principles, pitfalls and (pre-) clinical progress. J. Controlled Release 2012, 161, 175–187.

(2). Caldorera-Moore M; Guimard N; Shi L; Roy K Designer nanoparticles: incorporating size, shape and triggered release into nanoscale drug carriers. Expert Opin. Drug Delivery 2010, 7, 479–495.

(3). Vannucci L; Lai M; Chiuppesi F; Ceccherini-Nelli L; Pistello M Viral vectors: a look back and ahead on gene transfer technology. New Microbiol. 2013, 36, 1–22. [PubMed: 23435812]

(4). Hefferon K Plant Virus Expression Vectors: A Powerhouse for Global Health. Biomedicines 2017, 5, 44.

(5). Bittner AM; Alonso JM; Górzny M; Wege C Nanoscale science and technology with plant viruses and bacteriophages. Subcell. Biochem 2013, 68, 667–702. [PubMed: 23737068]

(6). Shukla S; Eber FJ; Nagarajan AS; DiFranco NA; Schmidt N; Wen AM; Eiben S; Twyman RM; Wege C; Steinmetz NF The Impact of Aspect Ratio on the Biodistribution and Tumor Homing of Rigid Soft-Matter Nanorods. Adv. Healthcare Mater. 2015, 4, 874–882.

(7). Champion JA; Mitragotri S Role of target geometry in phagocytosis. Proc. Natl. Acad. Sci U. S. A 2006, 103, 4930–4934. [PubMed: 16549762]

(8). Namba K; Stubbs G Structure of tobacco mosaic virus at 3.6 A resolution: implications for assembly. Science 1986, 231, 1401–1406. [PubMed: 3952490]

(9). Schlick TL; Ding Z; Kovacs EW; Francis MB Dual-surface modification of the tobacco mosaic virus. J. Am. Chem. Soc 2005, 127, 3718–3723. [PubMed: 15771505]

(10). Gulati NM; Pitek AS; Czapar AE; Stewart PL; Steinmetz NF The in vivo fates of plant viral nano-particles camouflaged using self-proteins: overcoming immune recognition. Adv. Healthcare Mater 2018, 6, 2204.

(11). Pitek AS; Jameson SA; Veliz FA; Shukla S; Steinmetz NF Serum albumin 'camouflage' of plant virus based nanoparticles prevents their antibody recognition and enhances pharmacokinetics. Biomaterials 2016, 89, 89–97. [PubMed: 26950168]

(12). Bruckman MA; Kaur G; Lee LA; Xie F; Sepulveda J; Breitenkamp R; Zhang X; Joralemon M; Russell TP; Emrick T; Wang Q Surface Modification of Tobacco Mosaic Virus with "Click" Chemistry. ChemBioChem 2008, 9, 519–523. [PubMed: 18213566]

(13). Tian Y; Gao S; Wu M; Liu X; Qiao J; Zhou Q; Jiang S; Niu Z Tobacco Mosaic Virus-Based 1D Nanorod-Drug Carrier via the Integrin-Mediated Endocytosis Pathway. ACS Appl Mater. Interfaces 2016, 8, 10800–10807. [PubMed: 27062971]

(14). Bruckman MA; Czapar AE; VanMeter A; Randolph LN; Steinmetz NF Tobacco mosaic virus-based protein nanoparticles and nanorods for chemotherapy delivery targeting breast cancer. J. Controlled Release 2016, 231, 103–113.

(15). Le DHT; Lee KL; Shukla S; Commandeur U; Steinmetz NF Potato virus X, a filamentous plant viral nanoparticle for doxorubicin delivery in cancer therapy. Nanoscale 2017, 9, 2348–2357. [PubMed: 28144662]

(16). Aljabali AAA; Shukla S; Lomonossoff GP; Steinmetz NF; Evans DJ CPMV-DOX delivers. Mol. Pharm 2013, 10, 3–10. [PubMed: 22827473]

(17). Madden AJ; Oberhardt B; Lockney D; Santos C; Vennam P; Arney D; Franzen S; Lommel SA; Miller CR; Gehrig P; Zamboni WC Pharmacokinetics and efficacy of doxorubicin-loaded plant virus nanoparticles in preclinical models of cancer. Nanomedicine (London, U. K.) 2017, 12, 2519–2532.

(18). Czapar AE; Zheng YR; Riddell IA; Shukla S; Awuah SG; Lippard SJ; Steinmetz NF Tobacco Mosaic Virus Delivery of Phenanthriplatin for Cancer therapy. ACS Nano 2016, 10, 4119. [PubMed: 26982250]

(19). Wilhelm S; Tavares AJ; Dai Q; Ohta T; Audet J; Dvorak HF; Chan WCW Analysis of nanoparticle delivery to tumours. Nat. Rev. Mater 2016, 1, 16014.

(20). Pitek AS; Wen AM; Shukla S; Steinmetz NF The Protein Corona of Plant Virus Nanoparticles Influences their Dispersion Properties, Cellular Interactions, and In Vivo Fates. Small 2016, 12, 1758–1769. [PubMed: 26853911]

(21). Schnitzer JE gp60 is an albumin-binding glycoprotein expressed by continuous endothelium involved in albumin trans- cytosis. Am. J. Physiol 1992, 262, H246–H254. [PubMed: 1733316]

(22). Chang C-H; Yen M-C; Liao S-H; Hsu Y-L; Lai C-S; Chang K-P; Hsu Y-L Secreted Protein Acidic and Rich in Cysteine (SPARC) Enhances Cell Proliferation, Migration, and Epithelial Mesenchymal Transition, and SPARC Expression is Associated with Tumor Grade in Head and Neck Cancer. Int. J. Mol. Sci 2017, 18, 1556.

(23). Prenzel KL; Warnecke-Eberz U; Xi H; Brabender J; Baldus SE; Bollschweiler E; Gutschow CA; Hölscher AH; Schneider PM Significant overexpression of SPARC/osteonectin mRNA in pancreatic cancer compared to cancer of the papilla of Vater. Oncol. Rep 2006, 15, 1397–1401. [PubMed: 16596217]

(24). Shi D; Jiang K; Fu Y; Fang R; Liu X; Chen J Overexpression of SPARC correlates with poor prognosis in patients with cervical carcinoma and regulates cancer cell epithelial- mesenchymal transition. Oncol. Lett 2016, 11, 3251–3258. [PubMed: 27123099]

(25). Desai N; Trieu V; Damascelli B; Soon-Shiong P SPARC Expression Correlates with Tumor Response to Albumin-Bound Paclitaxel in Head and Neck Cancer Patients. Transl. Oncol. 2009, 2, 59–64. [PubMed: 19412420]

(26). Chen B; Dai W; He B; Zhang H; Wang X; Wang Y; Zhang Q Current Multistage Drug Delivery Systems Based on the Tumor Microenvironment. Theranostics 2017, 7, 538–558. [PubMed: 28255348]

(27). Hoopes PJ; Wagner RJ; Duval K; Kang K; Gladstone DJ; Moodie KL; Crary-Burney M; Ariaspulido H; Veliz FA; Steinmetz NF; Fiering SN Treatment of Canine Oral Melanoma with Nanotechnology-Based Immunotherapy and Radiation. Mol. Pharm 2018, 15, 3717. [PubMed: 29613803]

(28). Bruckman MA; Jiang K; Simpson EJ; Randolph LN; Luyt LG; Yu X; Steinmetz NF Dual-modal magnetic resonance and fluorescence imaging of atherosclerotic plaques in vivo using vcam-1 targeted tobacco mosaic virus. Nano Lett. 2014, 14, 1551–1558. [PubMed: 24499194]

(29). Anderson EA; Isaacman S; Peabody DS; Wang EY; Canary JW; Kirshenbaum K Viral nanoparticles donning a paramagnetic coat: conjugation of MRI contrast agents to the MS2 capsid. Nano Lett. 2006, 6, 1160–1164. [PubMed: 16771573]

(30). Allen M; Bulte JWM; Liepold L; Basu G; Zywicke HA; Frank JA; Young M; Douglas T Paramagnetic viral nanoparticles as potential high-relaxivity magnetic resonance contrast agents. Magn. Reson. Med 2005, 54, 807–812. [PubMed: 16155869]

(31). Hu H; Zhang Y; Shukla S; Gu Y; Yu X; Steinmetz NF Dysprosium-Modified Tobacco Mosaic Virus Nanoparticles for Ultra-High-Field Magnetic Resonance and Near-Infrared Fluorescence Imaging of Prostate Cancer. ACS Nano 2017, 11, 9249–9258. [PubMed: 28858475]

(32). Geiger FC; Eber FJ; Eiben S; Mueller A; Jeske H; Spatz JP; Wege C TMV nanorods with programmed longitudinal domains of differently addressable coat proteins. Nanoscale 2013, 5, 3808–3816. [PubMed: 23519401]

(33). Li W; Griswold M; Yu X Rapid T1 mapping of mouse myocardium with saturation recovery Look-Locker method. Magn. Reson. Med 2010, 64, 1296–1303. [PubMed: 20632410]
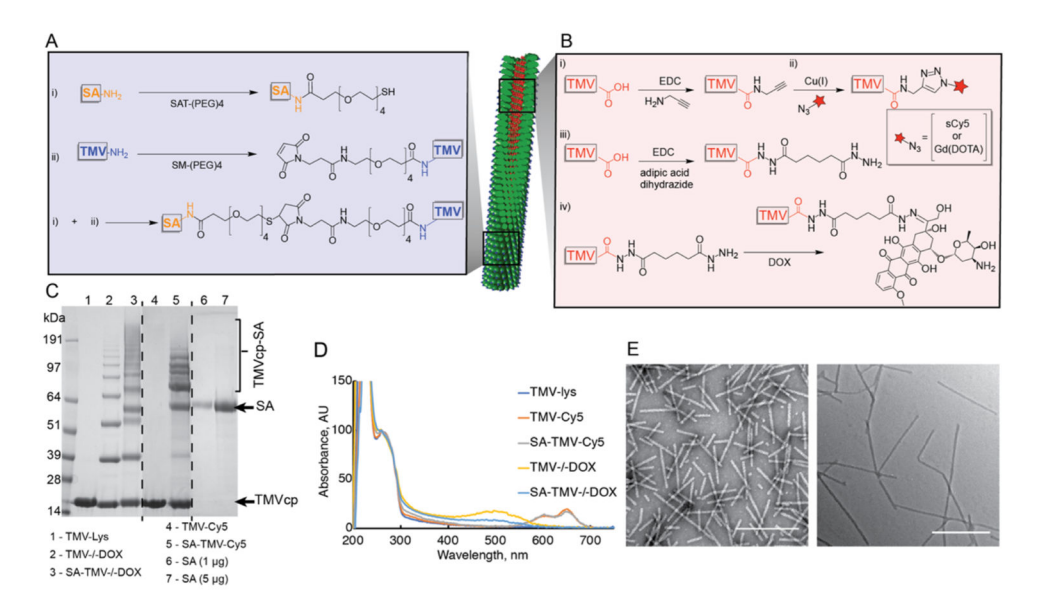
Figure 1.
Bioconjugation of SA and cargo molecules to TMV. (A) schematic representation of conjugation of SA to external surface of TMV-Lys and conjugation of Cy5, Gd(DOTA), and DOX to internal Glu residues of TMV: (i) conjugation of N-hydroxysuccinimide (NHS)-ester of SAT-(PEG)$_4$ to external amine groups of SA; (ii) conjugation of SM-(PEG)$_4$ to TMV's external Lys residues, followed by combining products (i + ii). (B) Schematic representation of conjugation of Cy5 or Gd(DOTA) and DOX to internal Glu residues of TMV: (i) 1-ethyl-3-(3-dimethylaminopropyl)carbodiimide (EDC) conjugation of propargyl amine to glutamic acid; (ii) alkyne–azide cycloaddition of Cy5-azide/GD(DOTA)-azide to product of reaction (i); (iii) EDC conjugation of adipic acid dihydrazide (AAD) to Glu; (iv) formation of hydrazone bond between DOX and the product of reaction (iii). (C) Sodium dodecyl sulfate-polyacrylamide gel electrophoresis (SDS-PAGE) analysis of TMV particles before and after conjugation. Successful conjugation of SA (M_w = 66 kDa; apparent M_w on the gel <64 kDa) to TMVcp (M_w = 17 kDa) in both SA-TMV-Cy5 and SA-TMV−/−DOX is indicated by the presence of multiple high molecular weight (>64 kDa) protein bands corresponding to SA-TMVcp conjugate (theoretical M_w of SA-TMVcp monomer is ~83 kDa). Free SA was used as a reference. (D) UV–vis spectra of TMV-Lys and its conjugates with Cy5, DOX, and SA. The spectra were normalized to A_{260}—maximum absorbance of TMV nucleic acid indicative of TMV concentration. Successful conjugation of Cy5 or DOX to internal cavity of TMV-Lys is indicated by the presence of absorbance peaks at 646 nm for Cy5 or 481 nm for DOX. (E) Transmission electron microscopy (TEM) images of SA-TMV-Cy5 (left) and SA-TMV−/−DOX (right) demonstrate structural integrity of TMV particles after the conjugation. Scale bars represent 500 nm.
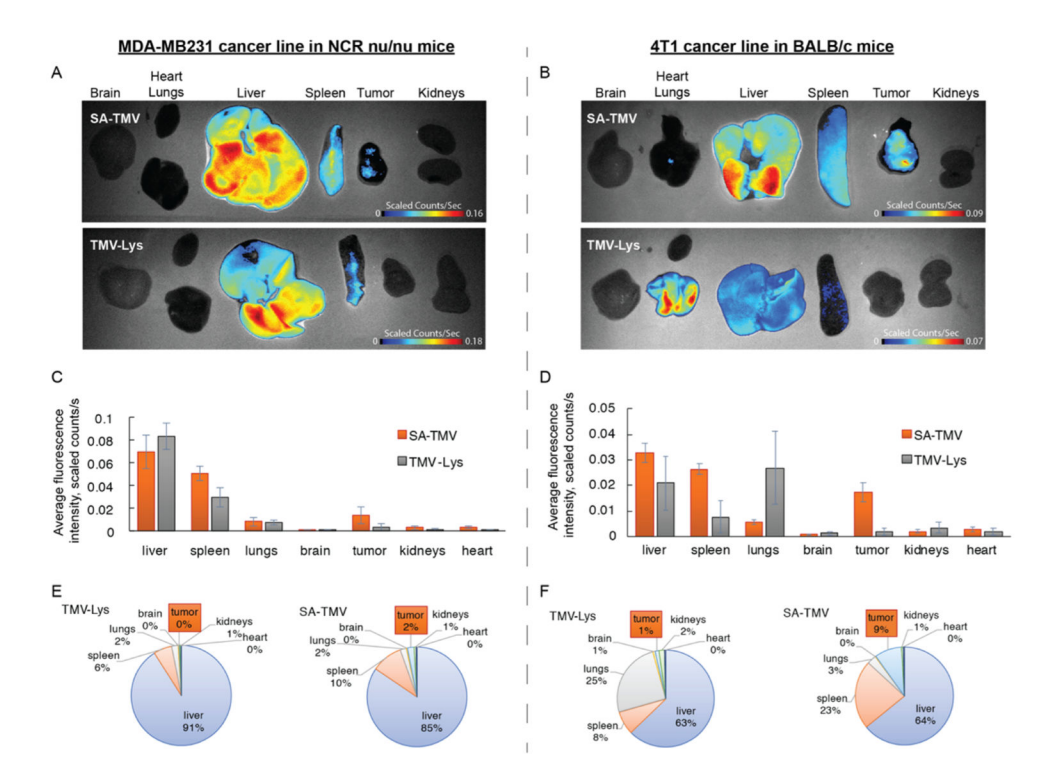
Figure 2.
In vivo biodistribution of SA-TMV-Cy5 vs TMV-Cy5 in murine models of MDA-MB-231 and 4T1 cancer. (A) Representative Maestro fluorescence images of biodistribution of SA-TMV-Cy5 particles in heterotopic model of human MDA-MB231 in NCR nu/nu mice (10 h post-i.v. administration). (B) Maestro fluorescence images of biodistribution of SA-TMV-Cy5 particles in heterotopic model of murine 4T1 in Balb/c mice. (C,D) Quantification of particle accumulation per unit area of different organs from panels A and B, respectively (i.e., average fluorescence signal per image pixel). (E,F) Quantification of % total particle accumulation in different organs in panels A and B, respectively (i.e., total fluorescence signal in each organ normalized to total fluorescence of all organs). SA stealth coating significantly improves accumulation of TMV particles in tumor mass in comparison to "bare" TMV particles.
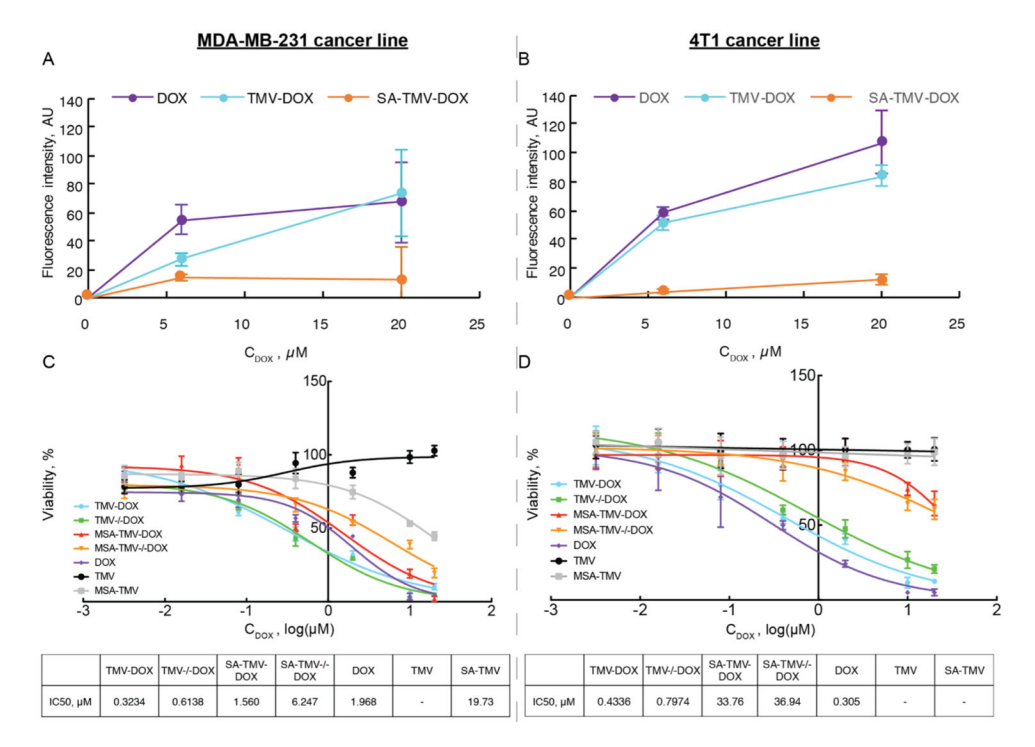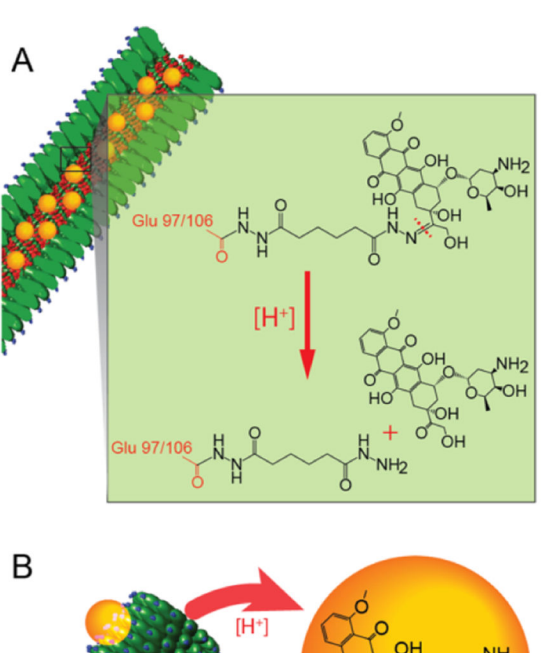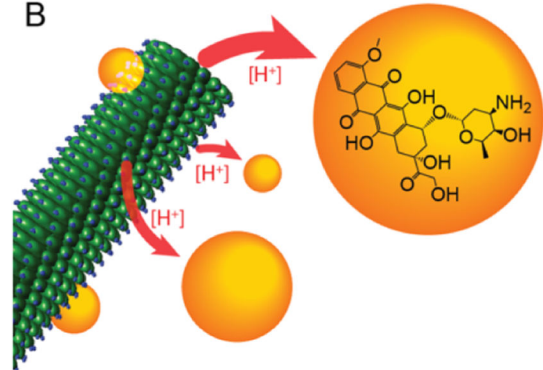
MDA-MB-231 cancer line

4T1 cancer line

	TMV-DOX	TMV-/-DOX	SA-TMV-DOX	SA-TMV-/-DOX	DOX	TMV	SA-TMV
IC50, μM	0.3234	0.6138	1.560	6.247	1.968	-	19.73

	TMV-DOX	TMV-/-DOX	SA-TMV-DOX	SA-TMV-/-DOX	DOX	TMV	SA-TMV
IC50, μM	0.4336	0.7974	33.76	36.94	0.305	-	-

Figure 3.

In vitro assays of nanoparticle uptake and cytotoxicity. (A,B) Quantification of cellular uptake of DOX, TMV-DOX, and SA-TMV-DOX in vitro in isolated MDA-MB231 and 4T1 cells, respectively. SA stealth coating decreases cellular internalization of therapeutic SA-TMV-DOX particles. (C,D) 3-[4,5-Dimethylthiazol-2-yl]-2,5 diphenyl tetrazolium bromide (MTT) viability and proliferation assay using MDA-MB231 and 4T1 cells, respectively. TMV-DOX, TMV–/–DOX, and SA-coated versions thereof were tested; free DOX, TMV, and SA-TMV were used as controls.
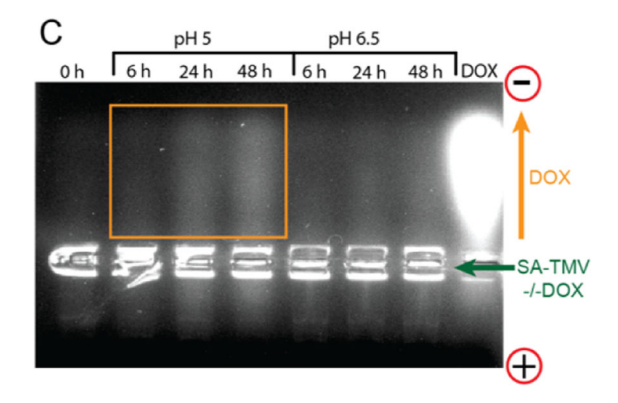
Figure 4.
pH-driven cleavage of DOX from SA-TMV-DOX particles. (A) Schematic representation of cleavage of pH-sensitive hydrazone bond between DOX and TMV (C=N double bond) in acidic conditions. (B) Schematic representation of DOX being released from the internal cavity of TMV upon cleavage of hydrazone link. (C) Agarose gel analysis of SA-TMV−/ −DOX samples after forced cleavage of DOX from TMV in acidic conditions (pH = 5 and pH = 6.5). The cleavage of DOX is indicated by increased fluorescence intensity in the top side of the gel proportional to incubation time in acidic conditions. Positively charged (free)

DOX molecules separate from TMV (unable to enter the pores of agarose gel) and travel toward negatively charged electrode (i.e., cathode). Free DOX was run as a reference.
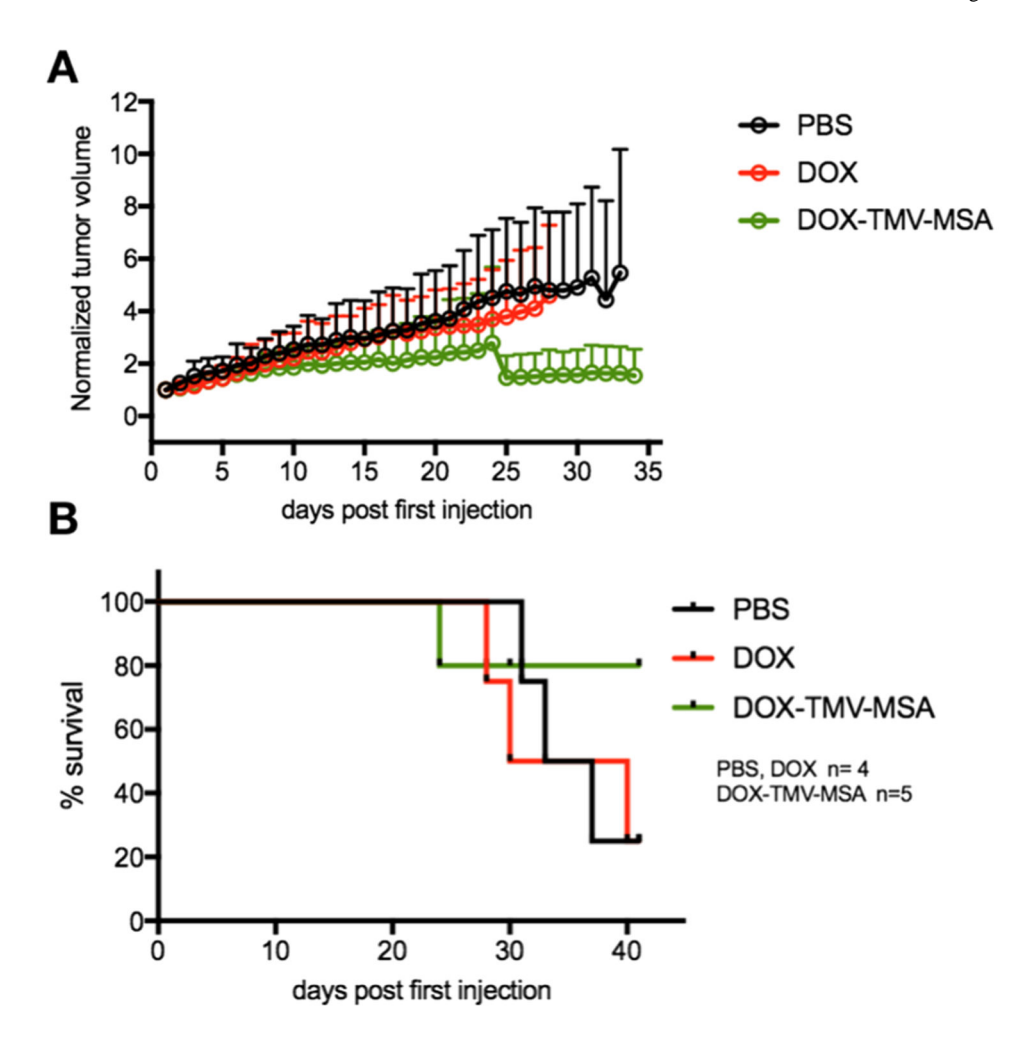
Figure 5.
In vivo efficacy of SA-TMV−/−DOX in MDA-MB231 mouse model. SA-TMV−/−DOX and free DOX were administered intravenously at a dose of 1 mg/kg every 3 days; a total of 10 treatments was given over a 4-week time course. One group of animals was treated with PBS. (A) Tumor growth curves, (B) survival plots.
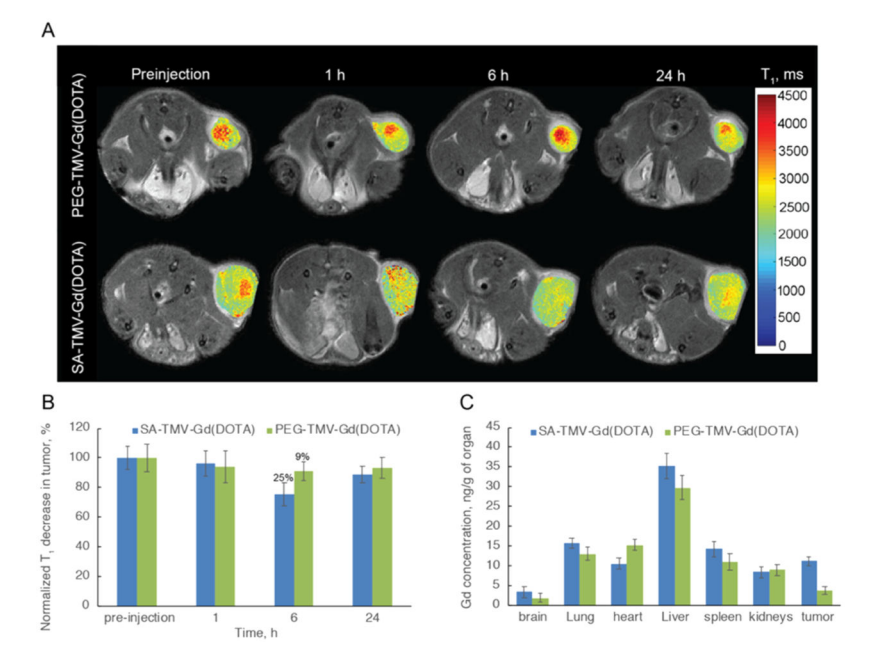
Figure 6.
In vivo diagnostics of PC3 tumor in NCR nu/nu mice by MRI and biodistribution of TMV-based contrast agents. (A) The SA-TMV-Gd(DOTA) brightened the PC3 tumor at 6 h after injection as compared with PEG-TMV-Gd(DOTA) contrast agent; slow recovery of T_1 relaxation times occurred 24 h post-injection. (B) Quantitative normalized T_1 decreased ~25% for SA-TMV-Gd(DOTA) at 6 h after injection and ~9% for PEG-TMV-Gd(DOTA) contrast agent. (C) Biodistribution of SA-TMV-Gd(DOTA) and PEG-TMV-Gd(DOTA) particles in NCR nu/nu mice bearing PC-3 tumor.

Table 1.

DLS Measurements of TMV Bioconjugates

sample	D_h	SD	PDI
TMV-Lys	243.0	1.3	0.197
SA-TMV-Cy5	221.6	2.9	0.234
SA-TMV–/–DOX	212	3.4	0.273